Journal of Magnetic Resonance 196 (2009) 149–156

Contents lists available at ScienceDirect

Journal of Magnetic Resonance

journal homepage: www.elsevier.com/locate/jmr

Optimal echo spacing for multi-echo imaging measurements of Bi-exponential T_2 relaxation

Adrienne N. Dula [a,b], Daniel F. Gochberg [b,c], Mark D. Does [a,b,c,*]

[a] Department of Biomedical Engineering, Vanderbilt University, Nashville, TN, United States
[b] Department of Radiology and Radiological Sciences, Vanderbilt University, Nashville, TN, United States
[c] Institute of Imaging, Vanderbilt University, Nashville, TN, United States

ARTICLE INFO

Article history:
Received 21 July 2008
Revised 14 October 2008
Available online 12 November 2008

Keywords:
MRI
Noise
Relaxometry
Myelin

ABSTRACT

Calculations, analytical solutions, and simulations were used to investigate the trade-off of echo spacing and receiver bandwidth for the characterization of bi-exponential transverse relaxation using a multi-echo imaging pulse sequence. The Cramer–Rao lower bound of the standard deviation of the four parameters of a two-pool model was computed for a wide range of component T_2 values and echo spacing. The results demonstrate that optimal echo spacing (TE_{opt}) is not generally the minimal available given other pulse sequence constraints. The TE_{opt} increases with increasing value of the short T_2 time constant and decreases as the ratio of the long and short time constant decreases. A simple model of TE_{opt} as a function of the two T_2 time constants and four empirically derived scalars is presented.

1. Introduction

Characterizing transverse relaxation with multiple exponentials, or a T_2 spectrum, is of interest in the study of various tissues and samples, including white matter and nerve [1,2], skeletal muscle [3,4], cerebral injury [5], tumor [6], plants [7], food [8], bone marrow [9,10], and more. Such characterization offers the potential to indirectly observe microscopic sample characteristics, such as myelin in white matter; however, it requires a relatively high signal-to-noise ratio (SNR) [11–13], so optimization of acquisition and processing methods is important.

Some studies have investigated optimal sampling of multi-exponential transverse relaxation, including numerical evaluations of number and range of echo times sampled [12–14] and the benefits of log-spaced sampling [15]. Beyond NMR-specific studies, there are a wealth of publications that address the fitting and parameter estimation from models involving the sum of exponential functions. An extensive review of this material was presented by Istratov and Vyvenko [16] and includes discussion on T_2-spectral resolution limits based on sampling times and model parameters. More recently, at least one publication presented simple analytical approximations of the uncertainty of fitted parameters in models of bi-exponential relaxation [17], which could be used to optimize sampling. A couple of studies have incorporated practical imaging factors/limitations—the effect of imperfect refocusing [18] and SAR limitations on sampling times [19]—into the process of optimizing sampling, but no study, to our knowledge, has incorporated the effect of receiver bandwidth on sampling times.

In a multi-echo imaging measurement, the time required for sampling each echo is typically on the order of milliseconds and can often place a lower limit on the echo spacing (TE). In order to reduce this time and, in-turn, TE, one must increase the receiver bandwidth (BW) at the cost of SNR. Herein is presented calculations and simulations that demonstrate the effect of trading-off BW for TE for two-pool systems with a range of possible relaxation rates and pool sizes.

2. Theory

As shown in Fig. 1, the minimum TE of a multi-echo imaging pulse sequence suitable for measuring transverse relaxation depends on the time required to acquire each echo (T_{acq}) and the time required for fixed events (T_{const}), like the RF refocusing pulse, spoiler gradients, ramp-time delays and delays for eddy current decay

$$TE = T_{const} + T_{acq} = T_{const} + N_s/BW, \tag{1}$$

where, N_s is the number of complex samples collected during each echo and BW is the bandwidth of this acquisition (assuming quadrature detection). Generally, every effort is made to minimize both T_{acq} and the T_{const} in order to minimize TE. Assuming one has defined a minimum N_s based on image resolution requirements, the only way to further reduce T_{acq} is to increase BW. The inherent trade-off in this reduction of T_{acq} is that the image SNR is inversely

* Corresponding author. Address: Vanderbilt University, Institute of Imaging Science, 1161 21st Avenue South, AA 1105 MCN, Nashville, TN 37232-2310, United States. Fax: +1 615 322 0734.
E-mail address: mark.does@vanderbilt.edu (M.D. Does).

1090-7807/$ - see front matter © 2008 Elsevier Inc. All rights reserved.
doi:10.1016/j.jmr.2008.11.002

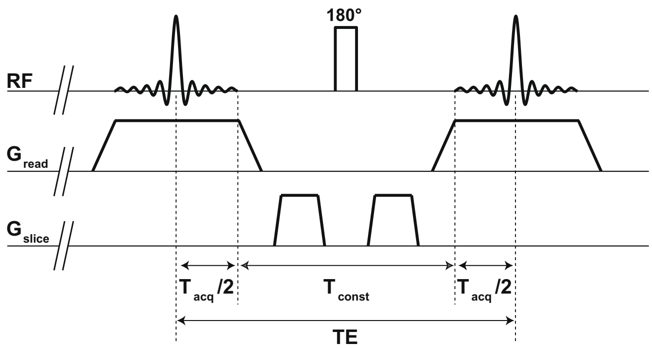

Fig. 1. Relevant timings of a multi-echo imaging pulse sequence. Two consecutive echoes are shown, separted by TE, one RF refocusing pulse, and two spoiler gradients.

proportional to the square root of *BW*, so reducing *TE* through increased *BW* also decreases the SNR. A reduced *TE* will improve the precision of estimated transverse relaxation parameters, while the concomitantly increased *BW* and subsequently decreased SNR will deteriorate this precision. Note that the exception to this description is when the total number of echoes (NE) is limited and the sample is comprised of a combination of spins with short and long T_2. In this case, reducing *TE* may reduce precision of fitted parameters as a consequence of under-sampling of long T_2 components. This problem may be avoided with minimal complication by appending a small number of widely spaced echoes at the end of the standard echo train [19]. For the purpose of the work herein, this under-sampling of long T_2 signal is avoided by assuming there is no practical limit on NE, so the analysis is focused on the trade-off of *TE* for image SNR.

In order to determine the optimal *TE* for a given system, the Cramer–Rao lower bound (CRLB) of the estimated relaxation parameter variance can be computed. A complete derivation of the Cramer–Rao lower bound can be found elsewhere [20], but a simple explanation in the context of this paper is as follows. Consider a two-pool system, in which the observed transverse magnetization is described by a simple real bi-exponential function with added white Gaussian noise,

$$M_T(n) = M_o^a \exp(-n \cdot TE/T_2^a) + M_o^b \exp(-n \cdot TE/T_2^b) + \varepsilon(n), \tag{2}$$

where $n = [1, 2, \ldots, NE]$, and $\varepsilon(n)$ are independent and identically distributed random values drawn from a Gaussian distribution with zero mean and standard deviation (SD) σ (i.e., the image noise). Unbiased estimates of the four model parameters, $M_o^a,\ M_o^b,\ T_2^a,$ and T_2^b, result from a least-squares fitting of the model to a series of observations, $M_T(n)$. Then the CRLB of the SD of the k-th of these fitted parameters, $s(\theta_k)$, is defined by

$$s(\theta_k) = \sqrt{(\mathbf{F}^{-1})_{kk}}, \tag{3}$$

where θ_k represents the k-th fitted parameter and $\mathbf{F}$ is the Fisher information matrix given by

$$F_{jk} = \frac{1}{\sigma^2} \sum_n \left(\frac{\partial M_T(n)}{\partial \theta_j} \frac{\partial M_T(n)}{\partial \theta_k} \right). \tag{4}$$

That is, the unbiased estimate of parameter θ_k has an associated variance that is no less than $s^2(\theta_k)$, thereby defining the best precision possible in estimating each of the four model parameters, $M_o^a,\ M_o^b,\ T_2^a,$ and T_2^b. The elements inside the summation in Eq. (4) are easily defined algebraically for the bi-exponential system in Eq. (2), and, using Eq. (1), *TE* and σ are related by,

$$\sigma = \sigma_0 \sqrt{BW/BW_0} = \sigma_0 \sqrt{\frac{N_s}{(TE - T_{\text{const}})BW_0}}, \tag{5}$$

where σ_0 defines the SD of the image noise at a receiver bandwidth of BW_0. From here, both numerical and analytical solutions of Eqs. (3)–(5) are possible, as are Monte Carlo simulations of fitting Eq. (2). All of these methods provide $s(\theta_k)$ as a function of the four sample parameters ($M_o^a,\ M_o^b,\ T_2^a$ and T_2^b), and the acquisition parameters (*NE*, *TE*, T_{const}, N_s, BW_0, and σ_0), although the CRLB solutions are closed form and much faster than using the Monte Carlo approach.

This work focuses on primarily on the numerical solutions, because of their ease and efficiency, but some Monte Carlo solutions and analytical solutions are presented for validation and generality. Simulations were also run to investigate the effect of *TE* when the underlying model is more complex than a sum of two discrete exponential functions. For example, in practice, most investigators characterizing transverse relaxation in white matter assume that the two commonly observed T_2 components have a finite width in T_2-space. Consequently, fitting of these data is usually done using a linear-inverse approach, where the observed signal is fitted to a wide range of decaying exponential functions and the solution (the T_2-spectrum) is regularized by minimizing its energy or curvature [11].

3. Methods

3.1. Numerical Solutions

As a starting point for numerical calculations, values of T_{const} = 5 ms, NE = 200, σ_0 = 1/750, Ns = 128, BW_0 = 64 kHz, M_o^a = 0.2, and M_o^b = 0.8 were used. This T_{const} value was based on a 1 ms RF refocusing pulse, two 1-ms spoiler gradients and two 1-ms delays after the spoiler gradients to allow eddy-currents to decay. (For more information on imaging pulse sequence requirements for measuring multi-exponential T_2, see [21] and [22], and related literature.) The effect of variations in T_{const} on the CRLB calculations is discussed further below. The relatively large *NE* value ensured that varying *TE* did not result in under-sampling of the longer-lived T_2 signal decay, which was tested by re-running a subset of CRLB calculations without using Eq. (5) to incorporate the effects of minimum *TE* on image noise (i.e., σ is constant)—see Fig. 2, in Results section. (Note that while *NE* = 200 may not be practical for most *in-vivo* imaging for reasons of power deposition and spoiler gradient demands, sampling to long echo times by appending a small number of widely spaced echoes at the end of a standard multi-echo sequence is practical and has the same effect of preventing under-sampling of long T_2 signal [19]). The values of the remaining acquisition parameters—σ_0, BW_0, Ns, M_o^a, and M_o^b—are arbitrary as they do not influence the optimization of *TE* v. *BW*—also demonstrated in Fig. 2, in the Results section.

With these parameters fixed, a series of calculations were performed with varied T_2^a, T_2^b and *TE*. The short-lived T_2 component was varied linearly as $T_2^a = [10, 11, \ldots, 35]$ ms, which spanned the expected range of T_2s for myelin water and intra-cellular muscle water. The long-lived relaxation time was varied in linear proportion to the short-lived time as $T_2^b = T_x \cdot T_2^a$, where $T_x = [3, 3.25, 3.5, \cdots, 10]$, which was more than sufficient to span the range of expected long-lived T_2 components in white matter, nerve, and muscle. For each pair of T_2^a and T_2^b, the Fisher Information matrix and resultant CRLB for estimated parameters' SD were computed using Eqs. (3)–(5) for $TE = [5.5, 5.6, 5.7, \cdots, 40]$ ms. The SNR of each fitted parameter was then defined as

$$SNR(\theta_k) = \theta_k / s(\theta_k). \tag{6}$$

3.2. Simulations

In order to validate these CRLB calculations and to explore a wider range of possible systems, a series of Monte Carlo simulations were performed. To validate the CRLB calculations, noisy bi-

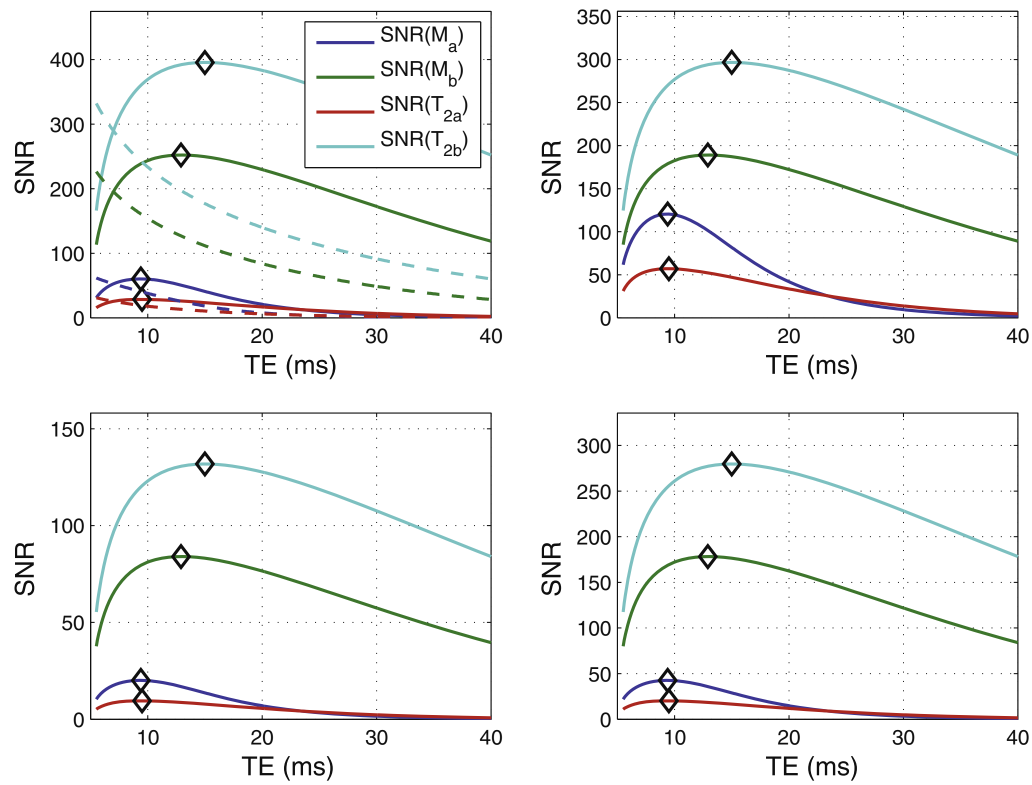

Fig. 2. Plots of SNR of four fitted parameters (indicated by line color) of a bi-exponential model of transverse relaxation as a function of *TE*. The zenith of each plot is indicated with a diamond symbol. In frame (a), calculations were made using T_2^a = 15 ms, T_2^b = 75 ms, T_{const} = 5 ms, *NE* = 200, σ_0 = 1/750, *Ns* = 128, BW_0 = 64 kHz, M_o^a = 0.2 and M_o^b = 0.8. Other frames show results from the same calculations made using the following different parameters: (b) M_o^a = 0.4 and M_o^b = 0.6, (c) σ_0 = 1/250, and (d) N_s = 256. Also shown in frame (a) as dashed lines are the results from the same calculations make without the use of Eq. (5)—i.e, no dependence of σ on *TE* (For interpretation of colour mentioned in this figure, the reader is referred to the web version of this article.).

exponential relaxation data were generated then fitted with Eq. (2) using a Levenberg–Marquardt algorithm. The initial guesses for the regression were randomly varied for each trial, with means equal to the underlying model parameters and a 10% coefficient of variation. These simulations used the following parameters: *NE* = 200, σ_0 = 1/750, *Ns* = 128, BW_0 = 64 kHz, M_o^a = 0.2, and M_o^b = 0.8, $T_2^a = [10, 15, 20, 25]$ ms, $T_x = [3, 4, 6, 8, 10]$, and $TE = [5.5, 6.0, 6.5, \cdots, 30]$ ms. Zero mean Gaussian noise ($\varepsilon(n)$, $n = 1, \ldots, NE$), with SD as defined by Eq. (5) were independently generated for N_t = 1000 trials, using each combination of T_2^a, T_x, and *TE*. The SNR for each parameter was then defined as the ratio of the parameter value to the SD of its fitted value calculated across the N_t trials, similar to Eq. (6).

Simulations were also run to investigate the effect of *TE* on model systems comprised of a distribution of relaxation times rather than two distinct components. In particular, the model described above was modified such that each spin pool was defined by a Gaussian shape in a log-spaced T_2 domain (similar to used in a previous study for fitting relaxation data [23]). That is, component *a* was defined by

$$S^a(j) = p^a \exp\left(-\left(\frac{\log T_2(j) - \log T_2^a}{\log d}\right)^2\right), \tag{7}$$

(where *log* is the natural logarithm) and likewise for $S^b(j)$, where *d* determines the width of the distribution, and p^a and p^b are set such that the sum of $S^a(j)$ and $S^b(j)$ over all *j = 1* to *J* equaled M_o^a and M_o^b, respectively. For all simulations, $T_2(j)$ was defined by *J* = 100 values, log-spaced between 5 ms and 1 s. With these distributions, the observed signal was then defined as

$$M_T(n) = \sum_{j=1}^{J} [(S^a(j) + S^b(j)) \exp(-n \cdot TE/T_2(j))] + \varepsilon(n). \tag{8}$$

The simulations used $T_2^a = 15$ ms, $T_x = [3, 4, 6, 10]$ $d = [1.0, 1.26, 1.59, 2.0]$, and 13 *TE* values pseudo-log-spaced between 5.5 ms and 30 ms. (Note that for the cases where *d* = 1.0, the T_2 component width was infinitely narrow and Eq. (2) was used to create $M_T(n)$). Fig. 6 shows the T_2 spectra (sum of $S^a(k)$ and $S^b(k)$) for each T_2^a, T_x, and *d*. All other parameters were the same as for the bi-exponential relaxation simulations, defined above. For every combination of T_x and *d*, noise, $\varepsilon(n)$, was independently generated for 1000 trials.

Each simulated noisy signal generated by Eq. (8) was fitted to a range of 100 T_2 values, log-spaced between 5 ms and 1 s using a non-negative least-square method [24] and regularized with a minimum curvature constraint [11]. The regularizing parameter was automatically adjusted using the generalized cross-validation approach [25]. Each spectrum was then analyzed by decomposing it into $n + 1$ T_2 components, where *n* was the number of spectral nadirs identified by positive to negative changes in the first derivative of the spectrum. After discarding T_2 components representing < 2% of the integrated spectral amplitude, if exactly two T_2 components were identified, then four model parameters, M_o^a, M_o^b, T_2^a, and T_2^b, were computed. Component amplitudes, M_o^a and M_o^b, were defined as the integrated area of each T_2 component and the component T_2 values, T_2^a, and T_2^b, were defined as the amplitude-weighted mean T_2 value computed over each component T_2 domain.

3.3. Analytical Solutions

The appendix outlines a general analytical solution for the standard deviation of each fitted parameter. The only approximation involved was to assume *NE* = ∞. This is equivalent to requiring that the decay of transverse magnetization be sampled down to the noise floor to avoid under-sampling of the long-lived T_2 component, as described above for the numerical calculations.

4. Results and discussion

Fig. 2a demonstrates typical CRLB-calculated graphs of $SNR(\theta_k)$ v. TE for each of the four fitted parameters for a system defined by $T_2^a = 15$ ms, $T_2^b = 75$ ms, $M_o^a = 0.2$, and $M_o^b = 0.8$. The solid lines are $SNR(\theta_k)$ values calculated using Eqs. (3)–(6), while the dashed lines are derived from the same calculation made while excluding the influence of BW on image noise (i.e, without Eq. (5)). The dashed lines decrease monotonically with TE, which agrees with previous work [14] (which used CRLB, but did not incorporate a BW–TE relationship) and demonstrates that under-sampling of long T_2 components was not a significant factor in the results presented herein. In contrast, for each fitted parameter, the solid lines show that $SNR(\theta_k)$ increases with TE to some maximal value, denoted in the figure by a diamond symbol, then decreases monotonically with further increasing TE. This demonstrates that the influence of echo spacing on BW and, in-turn, image noise, is an important factor in characterizing multi-exponential relaxation.

Also shown in Fig. 2 are similar graphs made from three variations in the sample or acquisition parameters: (b) $M_o^a = 0.4$ and $M_o^b = 0.6$, (c) $\sigma_0 = 1/250$, and (d) $N_s = 256$. In all cases, the optimal TE (TE_{opt}) for all four estimated parameters are identical to those in frame (a), demonstrating that the TE_{opt} calculations are independent of compartment sizes, baseline SNR, and number of samples. This independence from M_o^a, M_o^b, σ_0, and N_s can also be seen in the analytical solutions presented in the appendix, when combined with Eqs. 5 and 6. For example, Eq. (A.3) shows CRLB-defined minimum variance of all four model parameters. In each case, the parameters M_o^a, M_o^b, σ_0, and N_s are either not present or can be factored out. Therefore, each of these four parameters may change the scale of $s(\theta)$, but not the shape of its dependence on TE.

In addition to the numerical and analytical solutions, Monte Carlo simulations were also performed. Fig. 3 shows plots of $SNR(M_o^a)$ v. TE, derived from numerical CRLB calculations (lines) and the Monte Carlo simulations (dots) for the bi-exponential model given by Eq. (2). The results from the analytical solutions are not shown but would be indistinguishable from the numerical calculations. With the exception of a few measurements with low $SNR(M_o^a)$, the Monte Carlo- and CRLB-derived calculations are in good agreement, thereby validating the CRLB calculations and analytical solutions. In the cases where the Monte Carlo derived measures of $SNR(M_o^a)$ do not reach those determined from the CRLB (e.g., around TE = 18 ms in Fig. 3a), the difference likely results from very low SNR and, as a consequence, ineffective convergence to the true least-square solution in these cases.

Fig. 3 also demonstrates the strong dependence of TE_{opt} on both T_2^a and T_2^b. This is demonstrated by the solid line curves in Fig. 3, which show $SNR(M_o^a)$ for a wide array of different T_2^a and T_2^b values. Comparing data across the four frames shows that TE_{opt} increases with increasing T_2^a, while comparing data within each frame shows that TE_{opt} increases with decreasing T_2^b. The increase in TE_{opt} with increasing T_2^a is not surprising and simply indicates that a more slowly decaying function need not be sampled as quickly as a more quickly decaying function to produce the same variance of estimated parameters. The increasing TE_{opt} with *decreasing* T_2^b is, perhaps, less intuitive, and can be interpreted that SNR becomes increasingly more valuable as compared to temporal sampling density (i.e., echo spacing) when trying to distinguish signal components with increasingly similar T_2s.

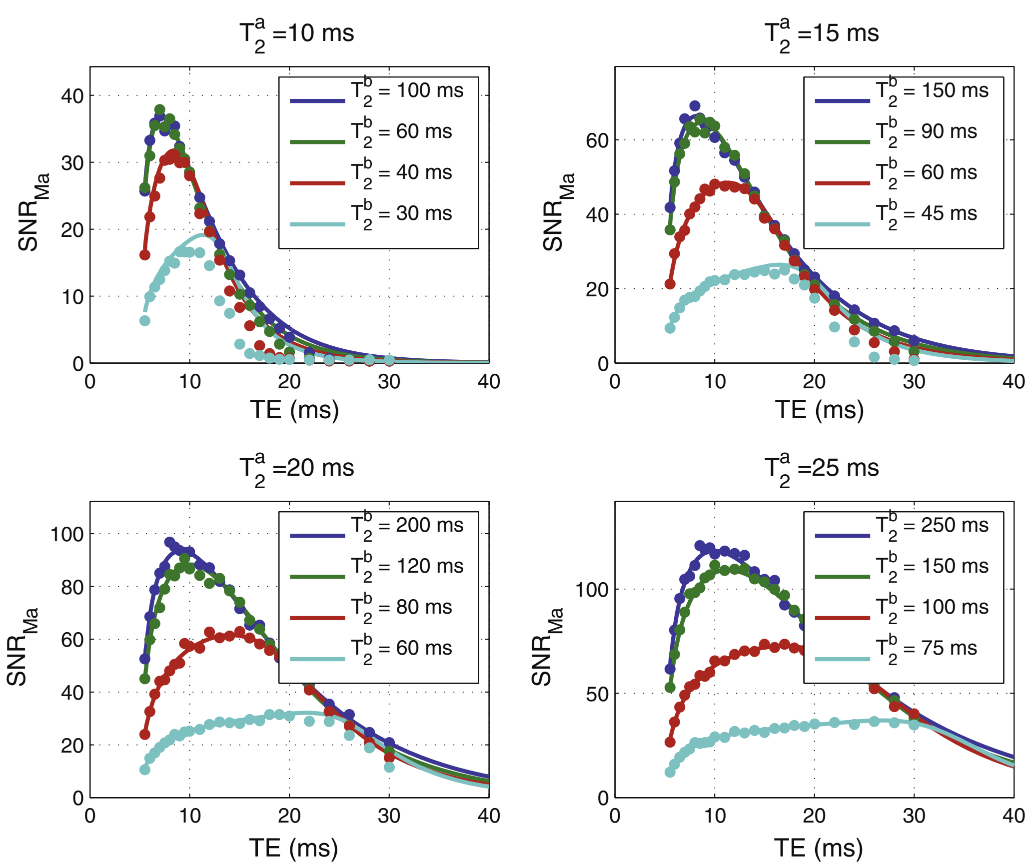

Fig. 3. Plots of $SNR(M_o^a)$ as a function of TE for a wide range of different T_2^a and T_2^b values. It is apparent that TE_{opt} increases with increases T_2^a and with decreasing T_2^b .

These CRLB calculations are relatively easy to compute for any given system of bi-exponential relaxation, but for a quick reference, the data from the calculations presented herein were used to generate a simple empirical model of the relationship between TE_{opt} and T_2^a and T_2^b. Fig. 4 shows a family of curves plotting TE_{opt} vs. T_2^a for all ratios T_2^a/T_2^b, from which it was observed that TE_{opt} increases approximately linearly with T_2^a

$$TE_{\mathrm{opt}} = m_1 T_2^a + b_1, \tag{9}$$

and the slope (m_1) and intercept (b_1) of these linear functions vary with T_2^a/T_2^b. Fig. 5 shows a crudely linear relationships between $\log(m_1)$ and T_2^a/T_2^b and between b_1 and T_2^a/T_2^b, and from these, Eq. (9) can be expanded to

$$TE_{\mathrm{opt}} \approx a_1 T_2^a \exp\left(m_2 \frac{T_2^a}{T_2^b}\right) + m_3\left(\frac{T_2^a}{T_2^b}\right) + b_3, \tag{10}$$

where $a_1 = \exp(b_2)$. Thus, three linear regressions were calculated to produce estimates of m_1, m_2, m_3, b_1, b_2, and b_3, resulting in the four independent constants in Eq. (10): a_1, m_2, m_3, and b_3. The same approach was used for all four estimated parameters in Eq. (1) (M_o^a, M_o^b, T_2^a, and T_2^b), and the results are shown in Table 1. Eq. (10) thus provides a quick and simple formula to estimate TE_{opt} for a given two-pool system and for a given parameter of interest.

In addition to the numerical studies, a complete analytical solution for $s(\theta_k)$ in the bi-exponential model is presented in the appendix. As mentioned above, the results match the numerical solutions and have the advantage of being applicable to arbitrary conditions, beyond those explored in this paper. These analytical results also provide insight into signal dependencies that are not readily apparent from the numerical results. For example, while the numerical results presented demonstrate that $s(M_o^a)$ increases as T_2^a approaches T_2^b, the analytical solution of $s(M_o^a)$ shows this effect quantitatively with the $(e^{-TE/T_2^a} - e^{-TE/T_2^b})^3$ term in the denominator. Similarly, one can see that the effect of similar T_2s is more pronounced for estimating component amplitudes than time constants.

In comparison to the analytical solutions presented herein, much simpler, although approximate, solutions have been derived using Bayesian probability theory [17]. These equations produce qualitatively similar curves to the dashed lines in Fig. 2, but when combined with Eq. (5) do not predict the existence of an optimal TE as found with the CRLB approach and validated with Monte Carlo, herein. Thus, while the CRLB solutions are complex analytically, they ultimately provide a more complete picture of the effect of model and acquisition parameters on estimated parameter variance.

A potential shortcoming of the CRLB solutions lies in the fact that a strict bi-exponential model, as defined by Eq. (2), is probably not a good representation of multi-exponential relaxation in many tissues and samples. A more relevant model is presented in Eq. (8), which generalizes the bi-exponential model to one defined by two smooth distributions of relaxation times, as shown in Fig. 6. Fig. 7 shows the results of the Monte–Carlo simulations of fitting data generated using these smooth T_2 spectra. (Note that these results were derived only from trials that resulted in two fitted T_2 components, which was > 88% of trials for all but three cases shown: $d = 1.59$, $T_2^a = 45$ ms, and $d = 2.00$, $T_2^a = 45$, and 60 ms.) The results demonstrate that, as expected, the CRLB calculations presented above do not predict the absolute value of the estimated parameter variances but they do predict the general shape and model parameter dependence of $SNR(M_o^a)$ vs. TE. Note similarity between Fig. 7a with Fig. 3b, which shows the results of fitting the same underlying bi-exponential data with a strict bi-exponential model (Fig. 3b) and with a distribution of T_2 times (Fig. 7a). Naturally, the strict bi-exponential fitting results in slightly higher $SNR(M_o^a)$ values, particularly at lower values of T_2^a/T_2^b, but the $SNR(M_o^a)$ vs. TE curve shape and TE_{opt} values are similar. Also, as the model T_2 components are broadened (increasing values of d, Fig. 7b–d), $SNR(M_o^a)$ values drop

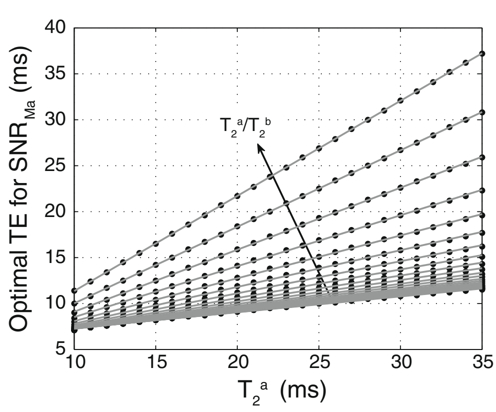

Fig. 4. A family of curves showing TE_{opt} vs. T_2^a for a wide range of T_2^a/T_2^b ratios. Each solid line is a best fitted linear function for a given T_2^a/T_2^b ratio.

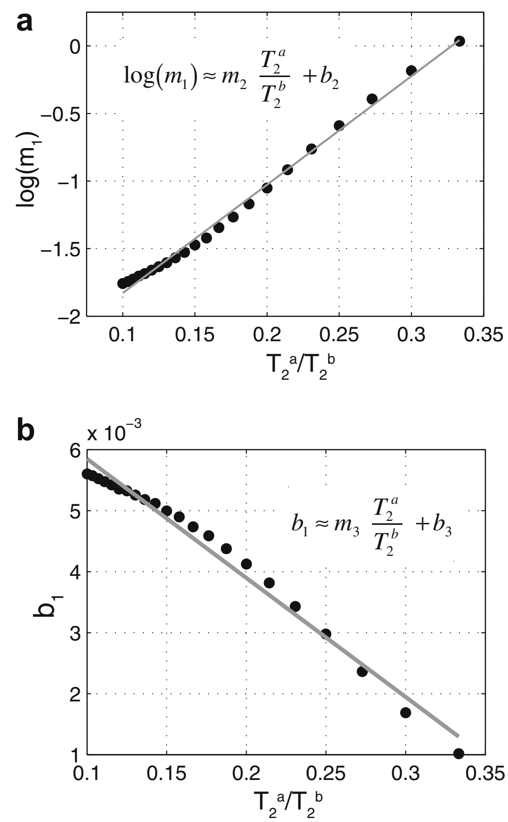

Fig. 5. (left) Plot of the natural logarithm of the slopes of the curves in Fig. 4 vs. T_2^a/T_2^b. The solid line shows the best fit linear function to these data as described by the equation in the frame. (right) Plot of the intercepts of the curves in Fig. 4 vs. T_2^a/T_2^b. The solid line shows the best fit linear function to these data as described by the equation in the frame.

Table 1
Constants computed for optimizing TE_{opt} with Eq. (8).

Parameter of interest	Constant in Eq. (8)			
	a_1	m_2	m_3 (s)	b_3 (s)
M_o^a	0.072	8.03	−0.020	0.0078
M_o^b	0.55	−1.98	−0.0086	0.0094
T_2^a	0.22	−0.11	−0.0009	0.0063
T_2^b	0.088	−2.35	−0.013	0.011

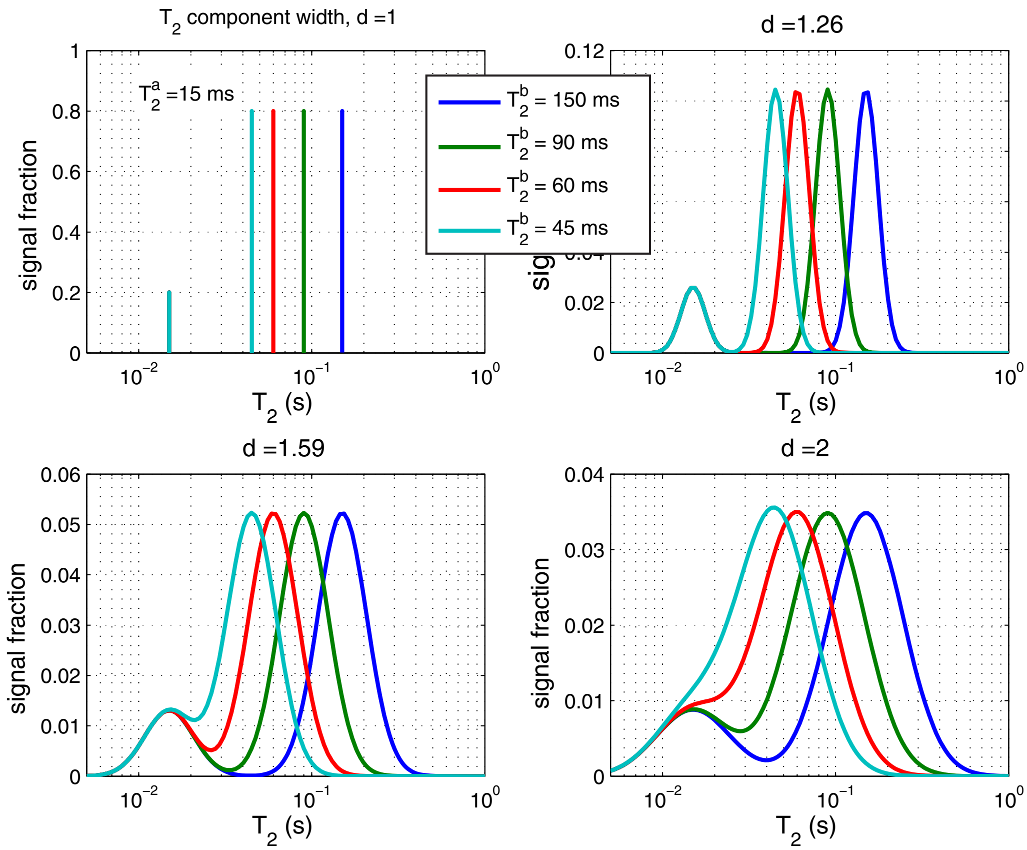

Fig. 6. T_2 spectra, defined using Eq. (7), used for Monte Carlo simulations of fitting data comprised of distributions of T_2 times. Shown in the four frames are spectra defined by T_2^a = 15 ms (all cases), four values of T_2^b, and four values of component width (d).

and the $SNR(M_o^a)$ v. TE curve broadens but the TE_{opt} values do not change appreciably.

A more general interpretation of the statistics of fitting smooth T_2 spectra is a complicated problem involving many factors. In addition to breadth of the T_2 components, as considered herein, the number and range of exponential functions to fit, the method of regularization, the adjustment of the regularizing parameter, and the method extracting model parameters from the spectrum may all significantly impact the results. Nonetheless, Eq. (10) appears to provide a good starting point for estimating TE_{opt} in systems that are thought to be well described by two relaxation components.

The utility of this work, through either the numerical or analytical solutions, is possibly most significant for myelin water mapping in white matter [26,22,27]. For these studies, a two-pool model is often used to describe water from within the layers of myelin as pool a and water from the intra- and extra-axonal spaces lumped together as pool b, and the relevant parameter for optimization is $SNR(M_o^a)$ because the myelin content is believed to be proportional to by M_o^a. In-vivo at 1.5T, the commonly cited values for T_2^a and T_2^b are 20 and 80 ms, respectively [27], which leads to TE_{opt} = 13.6 ms; however, this value drops closer to the typically used TE = 10 ms for smaller values of T_2^a as seen in experimental studies [22]. Also, although the TE_{opt} increases with increasing T_2^a and decreasing T_2^b, the $SNR(M_o^a)$ v. TE function also becomes more broad, so there is less at stake in optimizing the TE.

It is also important to note that the CRLB-derived values of TE_{opt} are not necessarily practical for any given imaging application. At low BW, imaging artifacts due to background field variation and chemical shift may limit the ability to effectively utilize the TE_{opt}. Also, depending on the application and hardware limitations, different T_{const} values may need to be considered. Longer T_{const} values will necessarily dictate longer TE_{opt} and CRLB calculations should be repeated for a condition where T_{const} is much different that 5 ms, as used herein. Lastly, the model assumed real data with additive Gaussian noise; however, at low SNR, the noise in magnitude MRI is Rician. For most cases of multi-exponential characterization, high SNR is required so the effect of noise fold-over in magnitude images is minimal. In general, though, one can correct for the effects of Rician noise on the echo magnitudes prior to data analysis [28], which will make the data analysis consistent with the CRLB calculations herein.

Acknowledgements

Grant Sponsors: NIH EB001744, EB001452, and NSF Career Award 0448915 (M.D.D). The authors thank Richard D. Dortch for processing code and Kenneth P. Whittall for helpful communications.

Appendix A

Starting with Eq. (2), and ignoring the noise term, the partial derivatives are

$$\frac{\partial M_T}{\partial M_0^a} = c_1^n \qquad \frac{\partial M_T}{\partial M_0^b} = c_2^n \qquad \frac{\partial M_T}{\partial T_2^a} = nc_3c_1^n$$
$$\frac{\partial M_T}{\partial T_2^b} = nc_4c_2^n \tag{A.1}$$

where

$$c_1 = e^{-TE/T_2^a} \quad c_2 = e^{-TE/T_2^b} \quad c_3 = \frac{TE\, M_0^a}{(T_2^a)^2} \qquad c_4 = \frac{TE\, M_0^b}{(T_2^b)^2}.$$

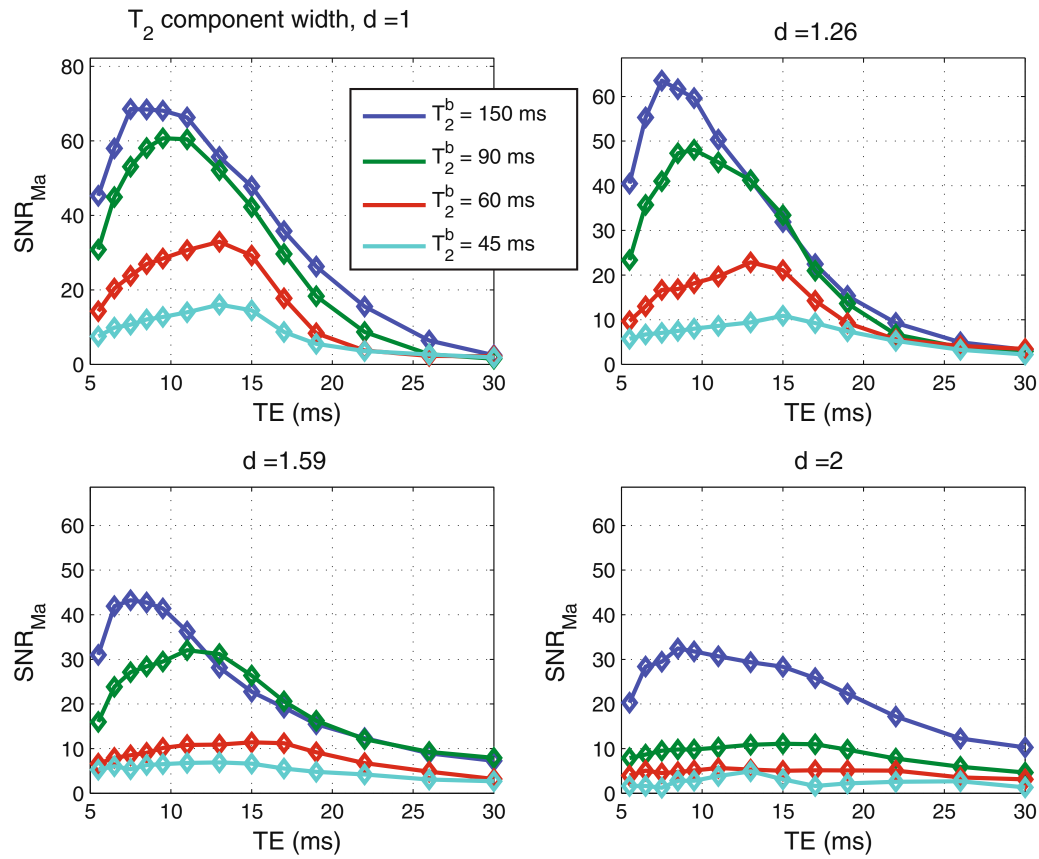

Fig. 7. Plots of $SNR(M_o^a)$ as a function of TE for cases where a distribution of T_2 times were fitted with a distribution of decaying exponential functions. Results are shown for a range of different T_2^b and component width (d) values.

Substituting this into Eq. (4), taking the number of echoes to infinity, and using the series formulae

$$\sum_{n=1}^{\infty} r^n = \frac{r}{1-r}, \ \sum_{n=1}^{\infty} n r^n = \frac{r}{(1-r)^2}, \text{ and } \sum_{n=1}^{\infty} n^2 r^n = \frac{r^2+r}{(1-r)^3}, \text{ we get}$$

$$F = \frac{1}{\sigma^2}\begin{bmatrix} \frac{c_1^2}{1-c_1^2} & & & \\ \frac{c_1c_2}{1-c_1c_2} & \frac{c_2^2}{1-c_2^2} & \ddots & \\ \frac{c_1^2c_3}{(1-c_1^2)^2} & \frac{c_1c_2c_3}{(1-c_1c_2)^2} & \frac{(c_1^4+c_1^2)c_3^2}{(1-c_1^2)^3} & \\ \frac{c_1c_2c_4}{(1-c_1c_2)^2} & \frac{c_2^2c_4}{(1-c_2^2)^2} & \frac{(1+c_1c_2)c_1c_2c_3c_4}{(1-c_1c_2)^3} & \frac{(c_2^4+c_2^2)c_4^2}{(1-c_2^2)^3} \end{bmatrix}. \tag{A.2}$$

Eq. (3) then gives

$$s^2(M_0^a) = \frac{-\sigma^2}{c_1^4(c_1-c_2)^6}(c_1^2-1)(c_1c_2-1)^2 \times \begin{pmatrix} c_2^2 + 2c_1c_2(c_2^2-3) + c_1^2(9-3c_2^2+c_2^4) - 4c_1^3(c_2+c_2^3) \\ +c_1^4(-11+21c_2^2-3c_2^4) + c_1^5(2c_2-6c_2^3) + c_1^6(4-7c_2^2+4c_2^4) \end{pmatrix}$$

$$s^2(M_0^b) = \frac{-\sigma^2}{c_2^4(c_1-c_2)^6}(c_1c_2-1)^2(c_2^2-1) \times \begin{pmatrix} c_1^2 + 2c_1(-3+c_1^2)c_2 + (9-3c_1^2+c_1^4)c_2^2 - 4c_1(1+c_1^2)c_2^3 \\ -(11-21c_1^2+3c_1^4)c_2^4 + (2c_1-6c_1^3)c_2^5 + (4-7c_1^2+4c_1^4)c_2^6 \end{pmatrix}$$

$$s^2(T_2^a) = \frac{-\sigma^2(c_1^2-1)^3(c_1c_2-1)^4}{c_1^4(c_1-c_2)^4c_3^2}$$

$$s^2(T_2^b) = \frac{-\sigma^2(c_1c_2-1)^4(c_2^2-1)^3}{(c_1-c_2)^4c_2^4c_4^2} \tag{A.3}$$

References

[1] C. Laule, I.M. Vavasour, S.H. Kolind, D.K. Li, T.L. Traboulsee, G.R. Moore, A.L. MacKay, Magnetic resonance imaging of myelin, Neurotherapeutics 4 (3) (2007) 460–484.
[2] C. Laule, I.M. Vavasour, B. Maedler, S.H. Kolind, S.M. Sirrs, E.E. Brief, A.L. Traboulsee, G.R.W. Moore, D.K.B. Li, A.L. MacKay, MR evidence of long T-2 water in pathological white matter, J. Magn. Reson. Imaging 26 (4) (2007) 1117–1121.
[3] G. Gambarota, B.E. Cairns, C.B. Berde, R.V. Mulkern, Osmotic effects on the T-2 relaxation decay of in vivo muscle, Magn. Reson. Med. 46 (3) (2001) 592–599.
[4] R.H. Fan, M.D. Does, Compartmental relaxation and diffusion tensor imaging measurements in vivo in lambda-carrageenan-induced edema in rat skeletal muscle, NMR Biomed. 21 (6) (2008) 566–573.
[5] A. Lascialfari, I. Zucca, M. Asdente, M. Cimino, U. Guerrini, R. Paoletti, E. Tremoli, V. Lorusso, L. Sironi, Multiexponential T_2-relaxation analysis in cerebrally damaged rats in the absence and presence of a gadolinium contrast agent, Magn. Reson. Med. 53 (6) (2005) 1326–1332.
[6] R.D. Dortch, T.E. Yankeelov, M.D. Does, Evidence of Multiexponential T_2 in Rat Glioblastoma. Proceedings of the ISMRM (Toronto) (2008) 1430.
[7] H. Van As, Intact plant MRI for the study of cell water relations, membrane permeability, cell-to-cell and long distance water transport, J. Exp. Bot. 58 (4) (2007) 743–756.
[8] A.M. Haiduc, J. van Duynhoven, Correlation of porous and functional properties of food materials by NMR relaxometry and multivariate analysis, Magn. Reson. Imaging 23 (2) (2005) 343–345.
[9] R.V. Mulkern, J.Q. Meng, K. Oshio, C.R.G. Guttmann, D. Jaramillo, Bone-marrow characterization in the lumbar spine with inner volume spectroscopic Cpmg imaging studies, JMRI—J. Magn. Reson. Imaging 4 (4) (1994) 585–589.
[10] A. Masumoto, S. Yonekura, M. Haida, N. Yanagimachi, T. Hotta, Analysis of intramedullary cell density by MRI using the multiple spin-echo technique, Am. J. Hematol. 55 (3) (1997) 134–138.
[11] K.P. Whittall, A.L. MacKay, Quantitative interpretation of NMR relaxation data, J. Magn. Reson. 84 (1) (1989) 134–152.

[12] S.J. Graham, P.L. Stanchev, M.J. Bronskill, Criteria for analysis of multicomponent tissue T_2 relaxation data, Magn. Reson. Med. 35 (3) (1996) 370–378.
[13] F.R. Fenrich, C. Beaulieu, P.S. Allen, Relaxation times and microstructures, NMR Biomed. 14 (2) (2001) 133–139.
[14] A. Anastasiou, L.D. Hall, Optimisation of T_2 and M0 measurements of bi-exponential systems, Magn. Reson. Imaging 22 (1) (2004) 67–80.
[15] R.I. Shrager, G.H. Weiss, R.G.S. Spencer, Optimal tine spacing for T_2 measurements: monoexponential and biexponential systems, NMR Biomed. 11 (1998) 297–305.
[16] A.A. Istratov, O.F. Vyvenko, Exponential analysis in physical phenomena, Rev. Sci. Instrum. 70 (2) (1999) 1233–1257.
[17] G.L. Bretthorst, How accurately can parameters from exponential models be estimated? A Bayesian view, Concept Magn. Reson. A 27A (2) (2005) 73–83.
[18] M.D. Does, J.C. Gore, Complications of non-linear echo time spacing for measurement of T_2, NMR Biomed. 13 (1) (2000) 1–7.
[19] M.G. Skinner, S.H. Kolind, A.L. MacKay, The effect of varying echo spacing within a multiecho acquisition: better characterization of long T_2 components, Magn. Reson. Imaging 25 (6) (2007) 840–847.
[20] S.M. Kay, Fundamentals of Statistical Signal Processing, Prentice-Hall, Englewood Cliffs, N.J, 1993.
[21] C.S. Poon, R.M. Henkelman, Practical T_2 quantitation for clinical applications, J. Magn. Reson. Imaging 2 (5) (1992) 541–553.
[22] K.P. Whittall, A.L. MacKay, D.A. Graeb, R.A. Nugent, D.K. Li, D.W. Paty, In vivo measurement of T_2 distributions and water contents in normal human brain, Magn. Reson. Med. 37 (1) (1997) 34–43.
[23] G.J. Stanisz, R.M. Henkelman, Diffusional anisotropy of T-2 components in bovine optic nerve, Magn. Reson. Med. 40 (3) (1998) 405–410.
[24] C.L. Lawson, R.J. Hanson, Solving Least Squares Problems, Prentice-Hall, Englewood Cliffs, NJ, 1974.
[25] G.H. Golub, M. Heath, G. Wahba, Generalized cross-validation as a method for choosing a good ridge parameter, Technometrics 21 (2) (1979) 215–223.
[26] A. MacKay, K. Whittall, J. Adler, D. Li, D. Paty, D. Graeb, In vivo visualization of myelin water in brain by magnetic resonance, Magn. Reson. Med. 31 (6) (1994) 673–677.
[27] C. Laule, E. Leung, D.K. Lis, A.L. Traboulsee, D.W. Paty, A.L. MacKay, G.R. Moore, Myelin water imaging in multiple sclerosis: quantitative correlations with histopathology, Mult. Scler. 12 (6) (2006) 747–753.
[28] J.M. Bonny, J.P. Renou, M. Zanca, Optimal measurement of magnitude and phase from MR data, J. Magn. Reson. B 113 (2) (1996) 136–144.